Degradation of Bone Quality in a Transgenic Mouse Model of Alzheimer's Disease

Joan E. LLabre[1,2], **Cristianel Gil**[3], **Neha Amatya**[3], **Sarita Lagalwar, PhD**[4], **Bernard Possidente, PhD**[3], **Deepak Vashishth, PhD**[1,2,*]

[1]Department of Biomedical Engineering, Rensselaer Polytechnic Institute, Troy, NY, USA

[2]Shirley Ann Jackson, Ph.D. Center for Biotechnology and Interdisciplinary Studies, Rensselaer Polytechnic Institute, Troy, NY, USA

[3]Department of Biology, Skidmore College, Saratoga Springs, NY, USA

[4]Neuroscience Program, Skidmore College, Saratoga Springs, NY, USA

Abstract

Alzheimer's disease (AD) patients present with symptoms such as impairment of insulin signaling, chronic inflammation, and oxidative stress. Furthermore, there are comorbidities associated with AD progression. For example, osteoporosis is common with AD wherein patients exhibit reduced mineralization, and a risk for fragility fractures. However, there is a lack of understanding on the effects of AD on bone beyond loss of bone density. To this end, we investigated the effects

accumulation of amyloidosis in brain correlated with an increase in several AGEs, consistent with a mechanistic link between elevated Aβ42 levels in the brain and AGE accumulation in bone.

Keywords

Alzheimer's Disease; 5XFAD Transgenic Mouse Model; Bone QCT/microCT; Glycoxidation; Biomechanics

Introduction

Alzheimer's disease (AD) is an irreversible and progressive form of dementia that affects over 50 million people worldwide [1]. While the pathology behind the neurodegeneration seen with AD is still not fully understood, there are two main proteins associated with the toxicity cascade, beta-amyloid and tau, which comprise the hallmarks of AD [2]–[7]. The abnormal processing of the amyloid precursor protein (*APP*) leading to accumulation of beta amyloid peptide (Aβ) results in plaques or clusters referred to as senile plaques (SPs) [2]. Meanwhile, the hyperphosphorylation of the intracellular microtubule-binding protein tau leads to an abundance of neurofibrillary tangles (NFTs) [3]. Moreover, AD patients present with myriad other symptoms such as cellular signaling dysregulation, impairment of insulin signaling, chronic inflammation, synapse loss, cellular metabolism disorders, and oxidative stress [4]–[7].

There are many contributing factors to AD occurrence, with research suggesting that lifestyle, environmental, and genetic factors all play an important role. For example, lifestyle habits such as high-fat diets (HFDs) and sleep fragmentation have been shown to increase chronic inflammation and, in turn, increase the risk of AD development [8], [9]. Certain mutations, such as *APP, PSEN1* and *PSEN2*, increase the risk for early-onset AD (EOAD) [10]. Whereas other genes, such as *APOE4*

Skeletal fragility is another severe comorbidity of AD with patients exhibiting an increased risk for fracture [21], [22

acclimated for 104 days. All mice were individually housed and provided with food (Prolab RMH 3000 Lab Diet pellets) and tap water were provided *ad libitum* and maintained under a controlled ambient temperature of 71 ± 2 °C and 12:12 LD schedule of indoor lighting (3500K fluorescent lamps, irradiance of approximately 70 μW.cm^{-2}) and provided with a 2g cotton Nestlet (Ancare Corporation, Bellmore, NY USA). From age 139 days to euthanization at 12 months of age, Nestlets were removed and a 4.5-in.-diamter running wheel was provided to assay voluntary circadian locomotor activity [41]. All experimental procedures were approved by the Skidmore College Animal Care and Use Committee and conformed to international ethical standards.

Nesting behavior and body mass

Approximately 30 grams of quilting cotton (Quilters Dream Cotton, 100% Pure Cotton, Virginia Beach, VA) was placed on top of each cage in the food bin on the first day of measurement. On the final day, the remaining cotton weight was subtracted from the initial weight to find the total amount of cotton used creating a nesting score. A baseline score was measured at 19-weeks, with follow-up scores at 26-, 33-, 40-, and 47-weeks of age. At these time intervals, the body mass of each mouse was also collected. Nesting behavior was measured for four days on some intervals, and five days on others. Therefore, all data shown has been standardized to represent 4-day scores.

Aβ42 ELISA

As previously reported [41], cortical brain tissue was harvested post-euthanasia and prepared according to the protocol established for 5XFAD mice [42]. Here, we breakdown the data to analyze sex differences, which has not previously been reported. The methods for the assay have been explained [42], and in brief, the tissue was flash frozen and re-suspended in PBS-0.5% Triton supplemented with protease inhibitors (A32965 ThermoFisher, Waltham, MA). Tissue was homogenized with a Corning Dounce homogenizer (1234F35 Thomas Scientific, Swedesboro, NJ). Cleared homogenates were supplemented with guanidine hydrochloride to a final concentration of 5M to solubilize plaques and then diluted in Standard Diluent Buffer. Aβ42 levels were measured in duplicates by the Invitrogen Human Aβ42 ELISA kit (KHB3441, ThermoFisher, Waltham, MA) and normalized by total protein content (5000002, Bio-Rad, Hercules, CA).

Micro-computed tomography

All femora, previously stored in saline at −80°C, were scanned using a μCT scanner (VivaCT40, Scanco Medical AG, Basserdoft, Switzerland), following guidelines by Bouxsein et al. [43]. High-resolution scans were acquired at 70 kVp energy, 114 mA current, 301 ms integration time using a 10.5 mm voxel size. Bone mineral density was calculated with a hydroxyapatite (HA) phantom used for calibration, and global threshold for all scans was set for 656 mg HA/cm^3 with a gaussian filtration (σ = 0.8, support = 1). Custom evaluation scripts with pre-defined volume of interest (VOI) were used to analyze the cortical and trabecular morphology of femora. Trabecular number, thickness and separation were calculated based on distance transformation, where 3D distances are estimated by fitting maximal spheres inside the structure or void space. Structural model

index and trabecular bone fraction were calculated based on triangularization of surface (i.e., one more interpolation step in comparison to counting voxels.

Cortical morphology was evaluated from 30 slices morphed from a ~0.3 mm region at mid-diaphysis. Variables collected were periosteal diameter, endosteal diameter, cortical thickness (Ct.Th), moment of inertia (I_{xx}), and cortical bone mineral density (BMD). To perform trabecular analysis, the most distal slice in which the condyles meet was identified and used as a point of reference. The VOI for trabecular analysis at the distal metaphysis was defined by first locating the growth plate in the distal end of the femora. Manual contouring was started 5 slices from it for a ~0.5mm region with contours every 10 slices and a 5% reduction to ensure no cortical bone was included in the analyses. Variables of interest were: bone trabecular thickness (Tb.Th), trabecular number (Tb.N), trabecular separation (Tb.Sp), volume fraction (BV/TV), structural model index (SMI), and trabecular BMD. Structural model index is measured as an indicator of the structure of trabeculae to estimate the plate- versus rod-like characteristic of the trabecular bone structure. This index was designed to be 0 for perfect plates, 3 for perfect rods, where plates are considered to be mechanically superior to rods. Reconstruction images (2D, 3D) were collected and recorded.

Confocal Raman spectroscopy

Femora were sectioned from the mid-diaphysis using a slow speed diamond saw. After drying, specimens were embedded in epoxy (EpoHeat CLR Resin & Hardener, Buehler, Lake Bluff, IL). Embedded specimens were transversely cut to produce ~500 μm sections that were subsequently polished with carbide (320 grit, 800 grit), and diamond (3 um) papers to achieve a smooth finish. Raman analysis was performed using a confocal Raman spectroscopy system (WITec Alpha 300R; WITec, Ulm, Germany) equipped with a 532 nm green laser. Confocal spectroscopy was selected as it allows for the magnification to be adjusted and the signal can reach beyond the surface level of the epoxy resin into the bone tissue, whereas non-confocal spectroscopy can only reach surface level and thus would be limited if samples are embedded.

An objective lens of 20x was first used to differentiate the bone tissue from epoxy resin (Figure 1A). Single spectrum at each morphological quadrant (N=4/sample) were

carboxymethyl-lysine (CML, 1150 cm^{-1}) [50] were measured and then used to analyze intensities of bone matrix composites.

Crystallinity was measured from the inverse of the FWHM of the $\nu_1PO_4^{3-}$ peak [45], [46], [52]. The mineral-to-matrix ratio (MMR) was calculated using polarization-dependent and -independent peaks, as the relative ratio between the ν_1PO_4 and Amide I and ν_2PO_4 and Amide III intensity peaks, respectively [45], [54]. Level of Type-B carbonate substitution was measured as the ratio between the ~1070 cm^{-1} carbonate subpeak and (ν_1) phosphate peaks [47], [53].

Glycation products, PEN and CML, were normalized to methylene [49], [50]. CML standard was purchased from Neta Scientific (MFCD04114278) and analyzed by confocal Raman spectroscopy to confirm the Raman marker band for CML (1150 cm^{-1}) in bone [50], [55].

X-ray diffraction

Femora were dissected with equal number of left or right femora randomly selected for each group. Soft tissues were removed, and all specimens were cleaned. Femora were cut at the ends using a slow speed (150 rpm) diamond saw blade (Buehler Isomet 100, Lake Bluff, IL) and the shaft was washed free of blood. Dry specimens, i.e. the whole cortical shaft (200 mg), were then powdered using a mortar and pestle. X-ray diffraction (XRD) patterns were obtained using the Panalytical X'Pert Diffractometer (Malvern Panalytical, Malvern, United Kingdom) operated at 45 kV and 40 mA with Copper (Cu) Kα with wavelength λ = 1.5405980 Å. Diffractograms were taken from 20 to 55° in a 2θ scale with a 0.01° step size and 499 s step count. Diffractograms were then analyzed using the HighScore software (Malvern Panalytical, Malvern, United Kingdom), where background subtraction and smoothing was done prior to peak fitting (Figure 2). The diffraction peak of 002, related to the length of the c-axis, was analyzed. The d-spacing and full width half-maximum (FWHM) of the 002 peak was calculated, and the mineral crystal size was determined using the Scherrer equation, $B = k\lambda/L\cos\theta$, as previously reported [58]–[61].

Fluorescent advanced glycation end-products

Total fAGEs in bone samples were measured using protocols previously established [62]–[66]. A section of cortical bone tissue was cut from the mid-diaphysis of each femora sample, with equal number of left or right femora randomly selected for each group, after mechanical testing. Each sample of approximately 10 mg was washed free of blood with distilled water and subsequently defatted in several cycles of 100% isopropyl ether to remove any outside fat or muscle tissue. All samples were then lyophilized to remove excess liquid from each bone sample. Each bone sample was then placed in a glass vial and submerged with 6N HCl solution at a ratio of 50 μL per 1 mg of bone. These were incubated at 110° C for direct hydrolysis to expose the bone proteins and lipids within the matrix. Two hydrolysates out of each sample were made by diluting the samples with nanopore water. These were used in two separate assays: a quinine sulphate fluorescence assay, and a collagen content assay.

The first assay used a quinine stock (1 μg Quinine/mL 0.1 M H_2SO_4) which was diluted with sulfuric acid to create standard curve. Triplicates of each standard and sample

hydrolysates were placed into the wells of a 96-microtiter plate. The fluorescence of each sample was measured using a spectrophotometer (Infinite 200, Tecan Trading AG, Switzerland) at 360 nm excitation and 460 nm emission.

The second part of the assay used a hydroxyproline stock (2000 μg L-hydroxyproline/mL 0.001 M HCl) diluted with nano-pure water to create a standard curve. Freshly made solutions of chloramine-T, 3.15 M perchloric acid, and p-dimethylaminobenzaldehyde (DMAB) were added to each standard and sample hydrolysate. After adding the chloramine-T solution, the samples were incubated at room temperature. Next, the 3.15 M perchloric acid solution was added, and the samples were incubated at room temperature. Finally, the DMAB solution was added, and the samples were incubated at 60°C. Triplicates of each standard and sample hydrolysate were placed in a 96-well plate. The absorbance of each sample was measured at 570 nm using the same spectrophotometer. The “in bulk” fAGEs content of each sample was then calculated as a unit of quinine fluorescence normalized by the collagen content (ng quinine/mg collagen).

Mechanical characterization

The contributions of AD to the biomechanical properties of bone were characterized using fracture mechanics-based tests for toughness. Fracture mechanics-based tests provide a measure of bone’s resistance to fracture due to a pre-existing flaw. Femora, with equal number of left or right femora randomly selected for each group, were prepared by first removing the femoral head and condyles and then forming a flaw, in the form of a controlled notch, at the mid-diaphyseal region on the anterior surface using a slow-speed diamond saw and sharpened using a razorblade. Three-dimensional reconstruction of the notch was performed using μCT images to measure the inner radius (Ri), outer radius (Ro), and notch angle with ImageJ, as the femora used for mechanical tests were the same as previously scanned with microCT. Samples were tested under wet conditions using an electromechanical testing system (EnduraTEC 3200, TA Instruments, New Castle, DE) at a ramp speed of 0.001mm/s with a span length of 6.5 mm. Load and displacement curves were recorded and using published equations [67], [68] we calculated initiation toughness (Kc, in; MPa√m) and maximum toughness (Kc, max; MPa√m). Initiation toughness defines the stress intensity at the initiation of fracture from the notch and the maximum toughness defines the stress intensity at maximum load during crack propagation (commonly referred to as crack growth resistance or propagation toughness).

Statistical analyses

Data presentation was generated using MATLAB R2020b (The MathWorks, Natick, MA). All data are displayed as boxplots with median and interquartile ranges with all data points scattered. The number next to each group in the legend indicates sample size (n). Statistical analyses were performed using R Project (https://www.rproject.org). Data were tested for normality using the Shapiro-Wilk test. In cases where data were slightly non-normal, we performed power transformations, such as the natural log, to normalize the distribution. Where data could not be normalized, non-parametric tests were used. Balanced data were tested for homoscedasticity using Bartlett’s test, while unbalanced data were tested using Fligner Killeen test which is a non-parametric test for homogeneity of group variances

based on ranks. Normal data were tested with Two-Factor ANOVA with Replication (α

Overall, all 5XFAD mice showed a 1.81% decrease in body mass at baseline that by 47-weeks had augmented to a 15.28% decrease in body mass pertaining to genotype, a common feature of AD progression [8], [70], [71].

5XFAD mice exhibited decline in nesting abilities

Nesting behavior was quantified by the grams of cotton used per each mouse over a course of four days, measured at baseline (19-weeks) and at the point of study culmination (47-weeks). Cotton usage showed large disparities as WT mice used large quantities of cotton whereas 5XFAD mice's usage continuously dropped to none or very little towards the

$\eta_p^2 = 5.45e\text{-}04$) on the periosteal diameter. Despite changes in the inner surface diameter, there were no significant changes in cortical thickness or moment of inertia with genotype or gender.

Bone density, measured by cortical BMD (Table 1), did not show genotype ($\chi^2(1) = 2.0629$, $p = 0.1509$, $\eta_p^2 = 0.03$) effects. However, cortical BMD did show a significant effect of gender ($\chi^2(1) = 5.8514$, $p = 0.01556$, $\eta_p^2 = 0.31$), wherein post hoc tests revealed female 5XFAD mice had a significant loss of BMD as they were differences between 5XFAD/ Female and WT/Female (

mice. No gender ($F_{1,16} = 1.741$, $p = 0.2055$, $\eta_p^2 = 0.10$) or interaction effects ($F_{1,16} = 0.281$, $p = 0.6031$) were present. Post hoc tests confirmed genotype effects within female groups ($p = 0.03703$) but not within male groups ($p = 0.148$).

We observed a significantly lower levels of mineralization in 5XFAD mice, as measured by the mineral-to-matrix ratio (MMR) calculated using polarization-dependent ($\nu_1PO_4^{3-}$/ Amide I) and -independent peaks ($\nu_2PO_4^{3-}$/Amide III). MMR1 (Figure 7C) showed significant genotype effects ($F_{1,16} = 26.593$, $p = 9.55e\text{-}05$, $\eta_p^2 = 0.61$) wherein 5XFAD mice displayed a significant loss of mineralization compared to WT mice. Post hoc tests confirmed genotype effects within female groups ($p = 0.002856$) and within male groups ($p = 0.0378$). No gender ($F_{1,16} = 0.973$, $p = 0.339$, $\eta_p^2 = 0.05$) or interaction effects ($F_{1,16} = 0.821$, $p = 0.378$) were present. MMR2 (Figure 7D) showed significant genotype effects ($\chi^2(1) = 12.623$, $p = 0.000381$, $\eta_p^2 = 0.58$) wherein 5XFAD mice displayed a significant reduction of mineralization compared to WT mice. Post hoc tests confirmed genotype effects within male groups ($p = 0.0011$) but not within female groups ($p = 0.0777$). No gender ($\chi^2(1) = 0.07$, $p = 0.978$, $\eta_p^2 = 0.05$) effects were present.

5XFAD mice showed accumulation of glycoxidation products

Confocal Raman spectroscopy was used to measure organic matrix characteristics of femoral cortical bone sections, in terms of glycoxidation products, such as carboxymethyl-lysine (CML) and pentosidine (PEN) (Figure 8).

CML (Figure 8A) showed significant genotype effects ($F_{1,16} = 86.430$, $p = 7.5e\text{-}08$, $\eta_p^2 = 0.84$) where in 5XFAD groups had significantly greater accumulation of CML compared to WT groups. Post hoc tests confirmed genotype effects within male groups ($p = 0.0000688$) and within female groups ($p = 0.0000177$). Gender effects ($F_{1,16} = 5.642$, $p = 0.0304$, $\eta_p^2 = 0.26$) were present but post hoc tests did not show individual differences between male and female groups. No interaction effects ($F_{1,16} = 0.285$, $p = 0.6009$) were present. PEN (Figure 8B) showed significant genotype effects ($F_{1,16} = 31.334$, $p = 4.01e\text{-}05$, $\eta_p^2 = 0.65$) where in 5XFAD groups had significantly greater accumulation of PEN compared to WT groups. Post hoc tests confirmed genotype effects within male groups ($p = 0.001247$) and within female groups ($p = 0.02484$). No gender ($F_{1,16} = 1.262$, $p = 0.278$, $\eta_p^2 = 0.07$) or interaction effects ($F_{1,16} = 1.093$, $p = 0.311$) were present.

5XFAD mice showed greater accumulation of fAGEs

compared to WT groups. Post hoc tests confirmed genotype effects within female groups ($p = 0.0000067$) and within male groups ($p = 0.0000829$). No gender ($F_{1,16} = 1.806$, $p = 0.198$, η_p^2

health [72]–[74]. Diminished nesting behavior has been demonstrated for other transgenic mouse models [73] but had not previously been documented for 5XFAD mice.

Metabolic markers of AD were not measured in this study but these have been previously reported for the model investigated here [8], [75]. For example, studies have shown that 5XFAD mice and other AD mice demonstrate a lean phenotype (i.e., weight loss, rise in metabolic rate, less white adipose tissue, lower leptin expression) and exhibit lower body weight compared to WT mice [8], [70], [71]. Similarly to this result, we observed a genotype effect with 5XFAD mice displaying reduced body mass compared to WT mice at 47 weeks of age. Of note, we included running wheels inside each mouse cage. While exercise might have mitigated or confounded these effects [76], there were no significant differences in the average running wheel activity levels (wheel revolutions per ten/min interval) between WT and 5XFAD mice. However, AD progression significantly diminishes motor control [77] which might have altered bone morphology.

Interestingly, the 5XFAD transgene construct [42] uses a modified *Thy1* gene promoter that is designed for brain-specific expression [78]. However, the *Thy1* gene downstream pathway can directly affect the Wnt signaling pathway which is responsible for bone formation [79]. Moreover, Aβ can interfere with the RANK downstream signaling [34] and stimulate osteoclast-specific genes [35]. In partial agreement with this observation, we found that bone structural properties in 5XFAD mice had a significant increase in inner surface expansion, while the outer surface remained unchanged. However, such changes were only seen in cortical, which demonstrated loss of BMD in a gender dependent manner, and not in distal trabecular femoral bone, as similarly reported in other AD mouse models [80], [81].

We evaluated surface level organic properties using confocal Raman spectroscopy, which uses frequency shifts corresponding to collagen and mineral characteristics of the bone matrix [40]–[53]. Glycoxidation products, such as carboxymethyl-lysine and pentosidine, are commonly seen to increase with higher levels of oxidation and glycation [82]–[85]. Although we did not measure inflammatory markers here, 5XFAD mice have been shown to have elevated oxidative stress and inflammation [8]. Furthermore, oxidative stress and systemic inflammation has been linked to formation of AGEs, and amyloid-beta [16], [86]. 5XFAD mice showed a significant increase in CML and PEN compared to WT mice. In addition, we observed a significant increase in total fAGEs, measured biochemically, in 5XFAD mice which could have impacted the plasticity potential of bone elevating the risk for fragility fractures.

When investigating bone toughness, we observed significant loss of initiation and maximum toughness in 5XFAD mice. Loss of toughness was significantly correlated with accumulation of all AGEs measured (i.e., CML, PEN, fAGEs), in line with several studies that have demonstrated AGE formation can reduce bone turnover and resistance to fracture [62]–[66]. In particular, the increased levels of AGEs have been found to cause a disruption in the alignment of the collagen fibril bundles consecutively reducing the amount of d-spacing available in the crystal lattice and thus leading to fragility fractures as energy dissipation is diminished [87]. We observed this in our study wherein XRD results

from 5XFAD mice bones showed a reduction in d-spacing and mineral crystal size, which correlated to loss of toughness.

We also evaluated surface level mineral compositional properties using confocal Raman spectroscopy. In concert with our XRD results, we observed a significant reduction of crystallinity in 5XFAD mice compared to WT groups. This loss of crystallinity is an indicator of a less perfect and more amorphous crystalline structure, which correlates to increased brittleness [45], [52]. It has been shown that Aβ can drive bone resorption by stimulating osteoclastic-specific genes [35], and consistent with this, we observed the presence of less mineralized bone tissue in 5xFAD mice bones, possibly due new bone formation following enhanced resorption [53], [54]. Furthermore, 5XFAD mice showed an increase in the carbonate-to-phosphate ratio, a measure of B-type carbonate substitutions, which is associated with a distortion of the atomic arrangement in the crystal lattice [47], [88], [89]. Overall, the mineral matrix of 5XFAD mice was shown to be highly affected in terms of quantity and quality (i.e., perfection, maturity, length).

We observed that CML and mineralization (as determined by the mineral-to-matrix ratio) correlated with initiation toughness. CML has been reported to have the ability of impacting the mineral phase of bone [82], [83], [90] and has been correlated with impaired mineralization [85]. In fact, it has been suggested that CML can attract positively charged calcium ions and cause increased mineralization, providing a link between the mineral and organic matrix of bone and subsequently minimize microdamage formation, energy dissipation and fracture toughness [91], [92]. Meanwhile, crystal size (as determined by

between AGE markers in bone and Aβ42 levels in brain must be further elucidated, we propose this association might provide clinically relevant. For example, the use of custom-

[7]. Gao C, Liu Y, Li L, and Hölscher C, “New animal models of Alzheimer’s disease that display insulin desensitization in the brain,” Rev. Neurosci, vol. 24, no. 6, pp. 607–615, 2013. [PubMed: 24259244]

[8]. Lin B, Hasegawa Y, Takane K, Koibuchi N, Cao C, and Kim-Mitsuyama S, “High-Fat-Diet Intake Enhances Cerebral Amyloid Angiopathy and Cognitive Impairment in a Mouse Model of Alzheimer’s Disease, Independently of Metabolic Disorders.,” J. Am. Heart Assoc, vol. 5, no. 6, Jun. 2016.

[9]. Phan TX and Malkani RG, “Sleep and circadian rhythm disruption and stress intersect in Alzheimer’s disease.,” Neurobiol. Stress, vol. 10, p. 100133, Feb. 2019. [PubMed: 30937343]

[10]. Lanoiselée H-M et al. , “APP, PSEN1, and PSEN2 mutations in early-onset Alzheimer disease: A genetic screening study of familial and sporadic cases.,” PLoS Med., vol. 14, no. 3, p. e1002270, Mar. 2017. [PubMed: 28350801]

[28]. Otero K et al. , “TREM2 and β-catenin regulate bone homeostasis by controlling the rate of osteoclastogenesis,” J Immunol, vol. 6, no. 6, pp. 247–253, 2009.

[29]. Frame G, Bretland KA, and Dengler-Crish CM, “Mechanistic complexities of bone loss in Alzheimer’s disease: a review.,” Connect. Tissue Res, vol. 61, no. 1, pp. 4–18, Jan. 2020. [PubMed: 31184223]

[30]. Libro R, Bramanti P, and Mazzon E, “The role of the Wnt canonical signaling in neurodegenerative diseases.,” Life Sci., vol. 158, pp. 78–88, Aug. 2016. [PubMed: 27370940]

[31]. Marzo A et al. , “Reversal of Synapse Degeneration by Restoring Wnt Signaling in the Adult Hippocampus.,” Curr. Biol, vol. 26, no. 19, pp. 2551–2561, Oct. 2016. [PubMed: 27593374]

[32]. Griciuc A et al. , “TREM2 Acts Downstream of CD33 in Modulating Microglial Pathology in Alzheimer’s Disease.,” Neuron, vol. 103, no. 5, pp. 820–835.e7, Sep. 2019. [PubMed: 31301936]

[33]. Cao X, “RANKL-RANK signaling regulates osteoblast differentiation and bone formation.,” Bone research, vol. 6. p. 35, 2018. [PubMed: 3051 fhlateease7 ETEMC/P << /MCID 2 >> BDCBT /F2 9 T163in -c8

o61Tink4l. “Raman spec/PSt8tcB2lin.68315.781T2002019. [PubMe271583992]
[48]. Unal M, Uppuganti S, Timur S, Mahadevan-Jansen A, Akkus O, and Nyman JS, “Assessing matrix quality by Raman spectroscopy helps predict fracture toughness of human cortical bone.,” Sci. Rep, vol. 9, no. 1, p. 7195, May 2019. [PubMed: 31076574]

[49]. Gamsjaeger S, Robins SP, Tatakis DN, Klaushofer K, and Paschalis EP, “Identification of Pyridinoline Trivalent Collagen Cross-Links by Raman Microspectroscopy.,” Calcif. Tissue Int, vol. 100, no. 6, pp. 565–574, Jun. 2017. [PubMed: 28246932]

[50]. Rubin MR et al. , “Advanced glycation endproducts and bone material properties in type 1 diabetic mice,” PLoS One, vol. 11, no. 5, pp. 1–14, 2016.

[51]. Unal M and Akkus O, “Raman spectral classification of mineral- and collagen-bound water’s associations to elastic and post-yield mechanical properties of cortical bone.,” Bone, vol. 81, pp. 315–326, Dec. 2015. [PubMed: 26211992]

[52]. Khalid M, Bora T, Al Ghaithi A, Thukral S, and Dutta J, “Raman Spectroscopy detects changes in Bone Mineral Quality and Collagen Cross-linkage in Staphylococcus Infected Human Bone.,” Sci. Rep, vol. 8, no. 1, p. 9417, Jun. 2018. [PubMed: 29925892]

[67]. Ritchie RO, Koester KJ, Ionova S, Yao W, Lane NE, and Ager JW 3rd, “Measurement of the toughness of bone: a tutorial with special reference to small animal studies.,” Bone, vol. 43, no. 5, pp. 798–812, Nov. 2008. [PubMed: 18647665]

[68]. Vashishth D, “Small animal bone biomechanics,” Bone, vol. 43, no. 5, pp. 794–797, 2008. [PubMed: 18672104]

[87]. Poundarik AA et al. , “A direct role of collagen glycation in bone fracture.,” J. Mech. Behav. Biomed. Mater, vol. 52, pp. 120–130, Dec. 2015. [PubMed: 26530231]

[88]. Taylor EA, Mileti CJ, Ganesan S, Kim JH, and Donnelly E, “Measures of Bone Mineral Carbonate Content and Mineral Maturity/Crystallinity for FT-IR and Raman Spectroscopic Imaging Differentially Relate to Physical–Chemical Properties of Carbonate-Substituted Hydroxyapatite,” Calcif. Tissue Int, vol. 109, no. 1, pp. 77–91, 2021. [PubMed: 33710382]

[89]. Awonusi A, Morris MD, and Tecklenburg MMJ, “Carbonate assignment and calibration in the Raman spectrum of apatite.,” Calcif. Tissue Int, vol. 81, no. 1, pp. 46–52, Jul. 2007. [PubMed: 17551767]

[90]. Sroga GE and Vashishth D, “Controlled Formation of Carboxymethyllysine in Bone Matrix through Designed Glycation Reaction.,” JBMR plus, vol. 5, no. 11, p. e10548, Nov. 2021. [PubMed: 34761150]

[91]. Diab T, Sit S, Kim D, Rho J, and Vashishth D, “Age-dependent fatigue behaviour of human cortical bone.,” Eur. J. Morphol, vol. 42, no. 1–2, pp. 53–59, 2005. [PubMed: 16123024]

[92]. Ural A and Vashishth D, “Hierarchical perspective of bone toughness – from molecules to fracture,” Int. Mater. Rev, vol. 59, no. 5, pp. 245–263, Jun. 2014.

[93]. O’Flaherty EJ, “Modeling normal aging bone loss, with consideration of bone loss in osteoporosis.,” Toxicol. Sci, vol. 55, no. 1, pp. 171–188, May 2000. [PubMed: 10788572]

[94]. Hemmati E, Mirghafourvand M, Mobasseri M, Shakouri SK, Mikaeli P, and Farshbaf-Khalili A, “Prevalence of primary osteoporosis and low bone mass in postmenopausal women and related risk factors.,” J. Educ. Health Promot, vol. 10, p. 204, 2021. [PubMed: 34395641]

[95]. Dhaliwal R, Ewing SK, Vashishth D, Semba RD, and V Schwartz A, “Greater Carboxy-Methyl-

Figure 1. Analysis of bone tissue by confocal Raman spectroscopy.

(A) Objective lens of 20x (left) was used to differentiate bone tissue (region marked ‘b’) from epoxy (region marked ‘a’) resin which was then confirmed at 100x (right). (B) Complete Raman spectrum collected from bone tissue.

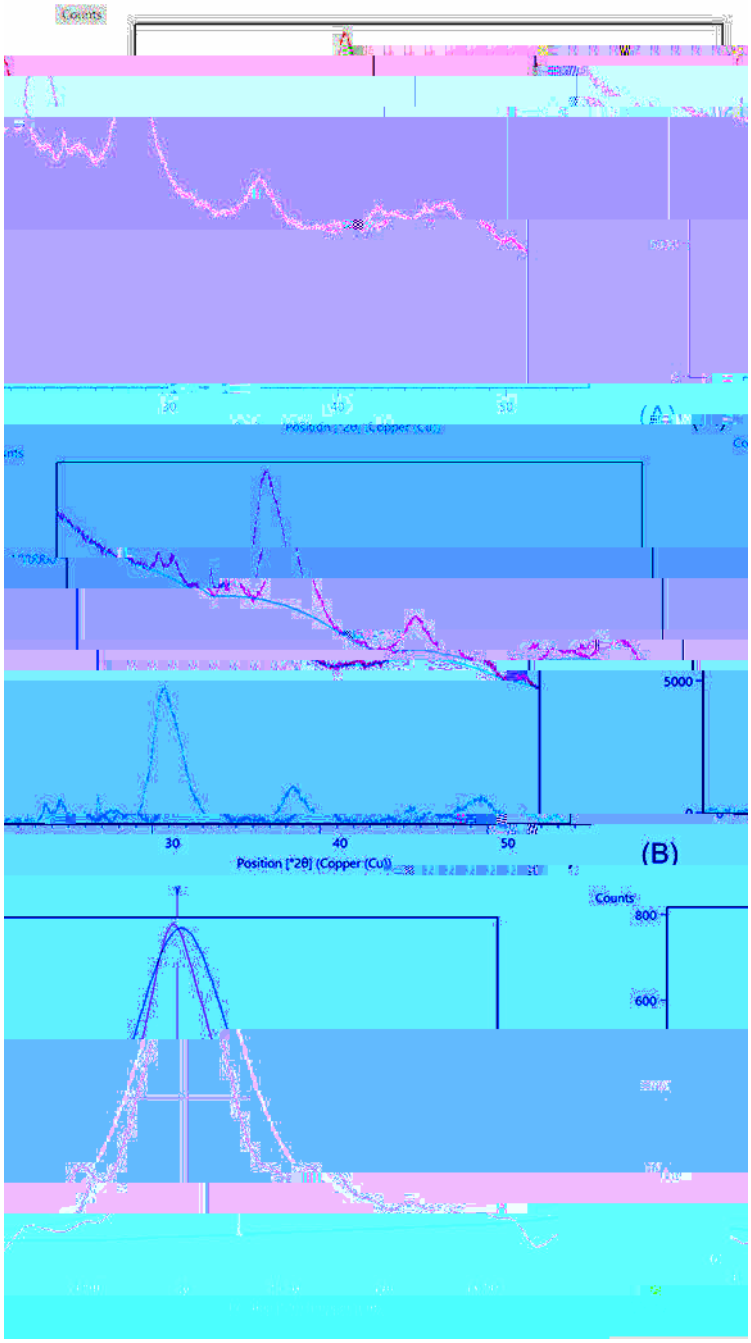

Figure 2. Analysis of bone powder by X-ray Diffraction.

(A) Raw peak intensities. (B) Baseline correction for XRD peak analysis. (C) Peak fitting of 002 peak.

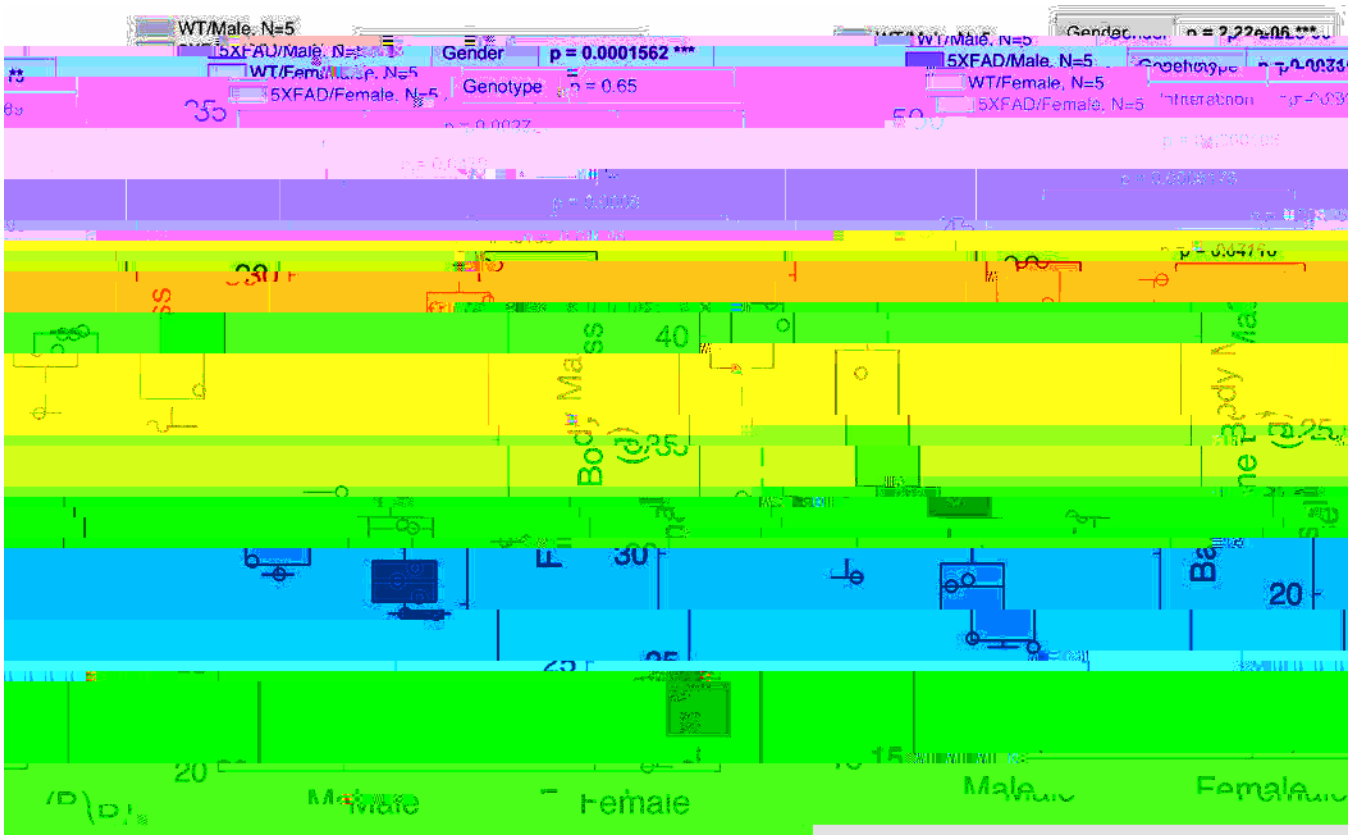

Figure 3. 5XFAD mice displayed a progressive weight loss.

5XFAD mice showed a 1.81% decrease in body mass at baseline (A) that by 47-weeks (B) had augmented to a 15.28% decrease. Results are shown as boxplots (with median and interquartile range) showing all data points. Statistically significant differences were determined by Kruskal–Wallis ($\alpha < 0.05$) test by ranks to discern gender, and genotype effects, with Dunn's test (95% CI) as post hoc tests in pairwise multiple comparisons procedure based on rank sums; or by Two-Factor ANOVA with Replication ($\alpha < 0.05$) to discern gender, genotype, and interactions effect, with Tukey's HSD test (95% CI) as post hoc tests in multiple comparisons of means. Significant codes: $p < 0.05$ '*', $p < 0.01$ '**', $p < 0.001$ '***'.

Figure 4. 5XFAD mice exhibited decline in nesting abilities.

(A) Example of near perfect nest building compared to an unidentifiable nest. AD progression significantly reduced the ability of 5XFAD mice to build nests exhibiting a decline from baseline (B) to the end of the study (C). Despite gender not being a significant factor in these changes, we did observe greater effect sizes within the female groups. Results are shown as boxplots (with median and interquartile range) showing all data points. Statistically significant differences were determined by Kruskal–Wallis ($\alpha < 0.05$) test by ranks to discern gender, and genotype effects, with Dunn's test (95% CI) as post hoc tests in pairwise multiple comparisons procedure based on rank sums. Significant codes: $p < 0.05$ '*', $p < 0.01$ '**', $p < 0.001$ '***'.

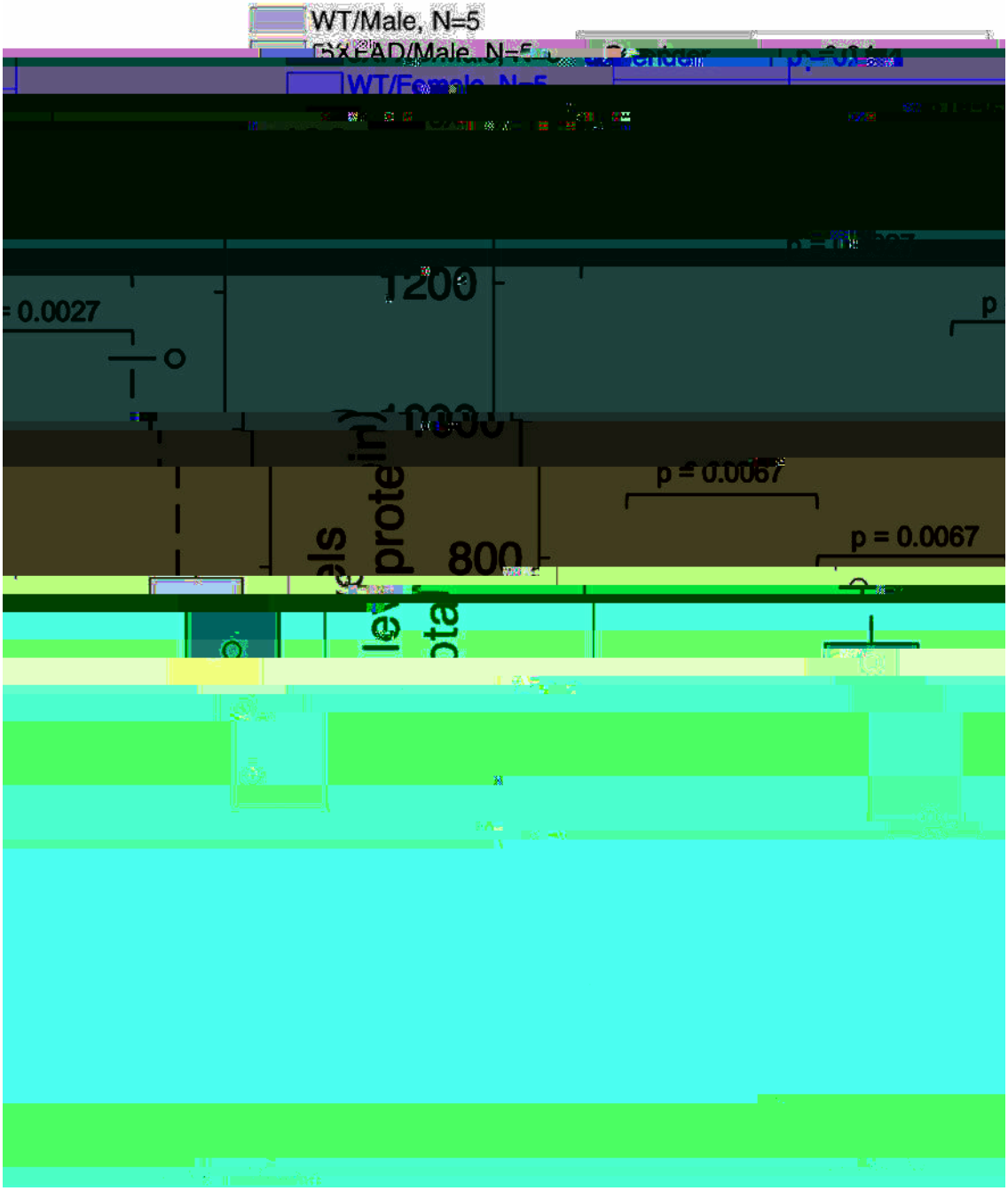

Figure 5. Elevated levels of Aβ42 in 5XFAD mice.

5XFAD mice showed a significant increase in Aβ42 levels compared to WT mice, regardless of gender. Results are shown as boxplots (with median and interquartile range) showing all data points. Statistically significant differences were determined by Kruskal–Wallis ($\alpha < 0.05$) test by ranks to discern gender, and genotype effects, with Dunn's test (95% CI) as post hoc tests in pairwise multiple comparisons procedure based on rank sums. Significant codes: $p < 0.05$ '*', $p < 0.01$ '**', $p < 0.001$ '***'.

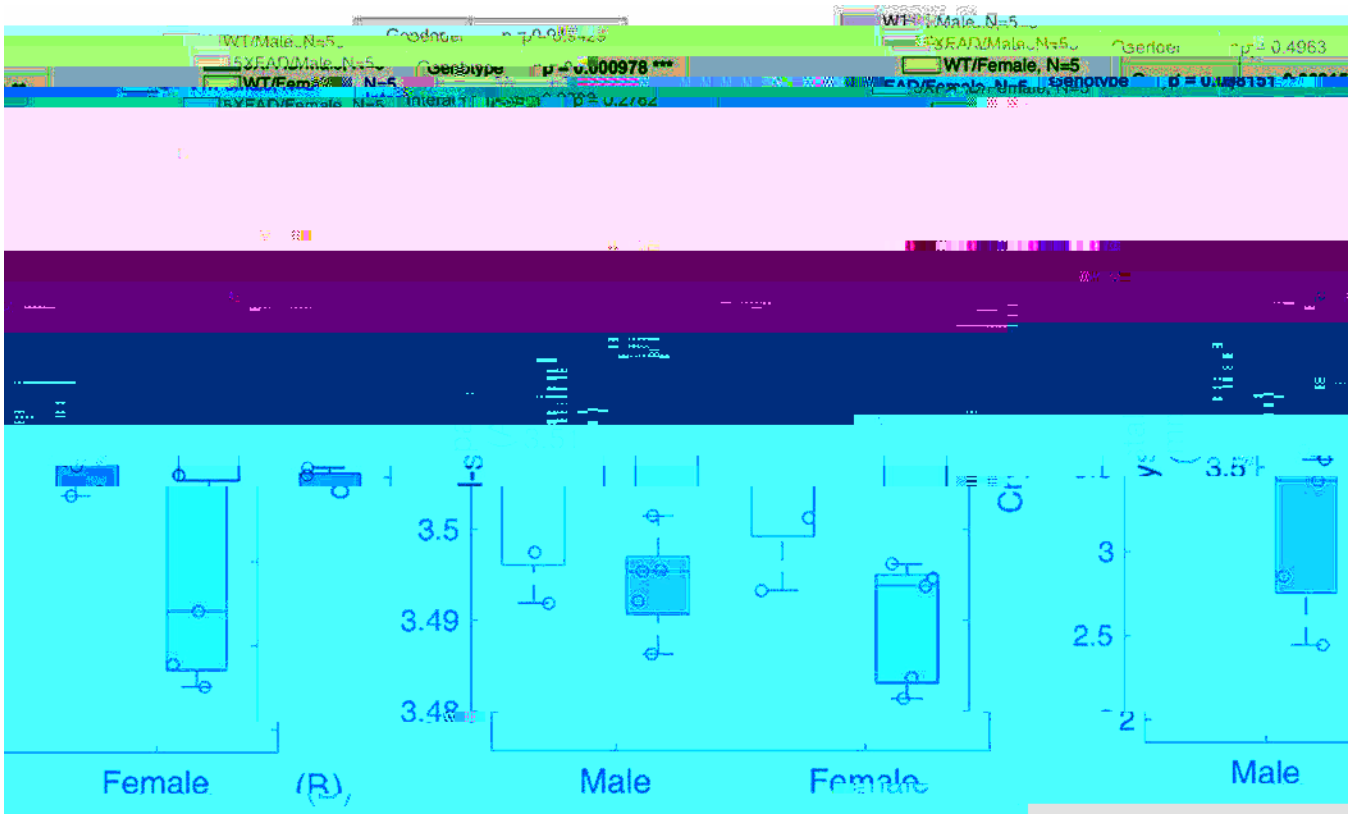

Figure 6. Diminished mineral crystal size and lattice d-spacing in 5XFAD mice.

The FWHM of peak 002 was used to calculate the mean crystal size (A) and d-spacing (B) of the mineral crystal lattice. Results are shown as boxplots (with median and interquartile range) showing all data points. Statistically significant differences were determined by Two-Factor ANOVA with Replication ($\alpha < 0.05$) to discern gender, genotype, and interactions effect, with Tukey's HSD test (95% CI) as post hoc tests in multiple comparisons of means; or by Kruskal–Wallis ($\alpha < 0.05$) test by ranks to discern gender, and genotype effects, with Dunn's test (95% CI) as post hoc tests in pairwise multiple comparisons procedure based on rank sums. Significant codes: $p < 0.05$ '*', $p < 0.01$ '**', $p < 0.001$ '***'.

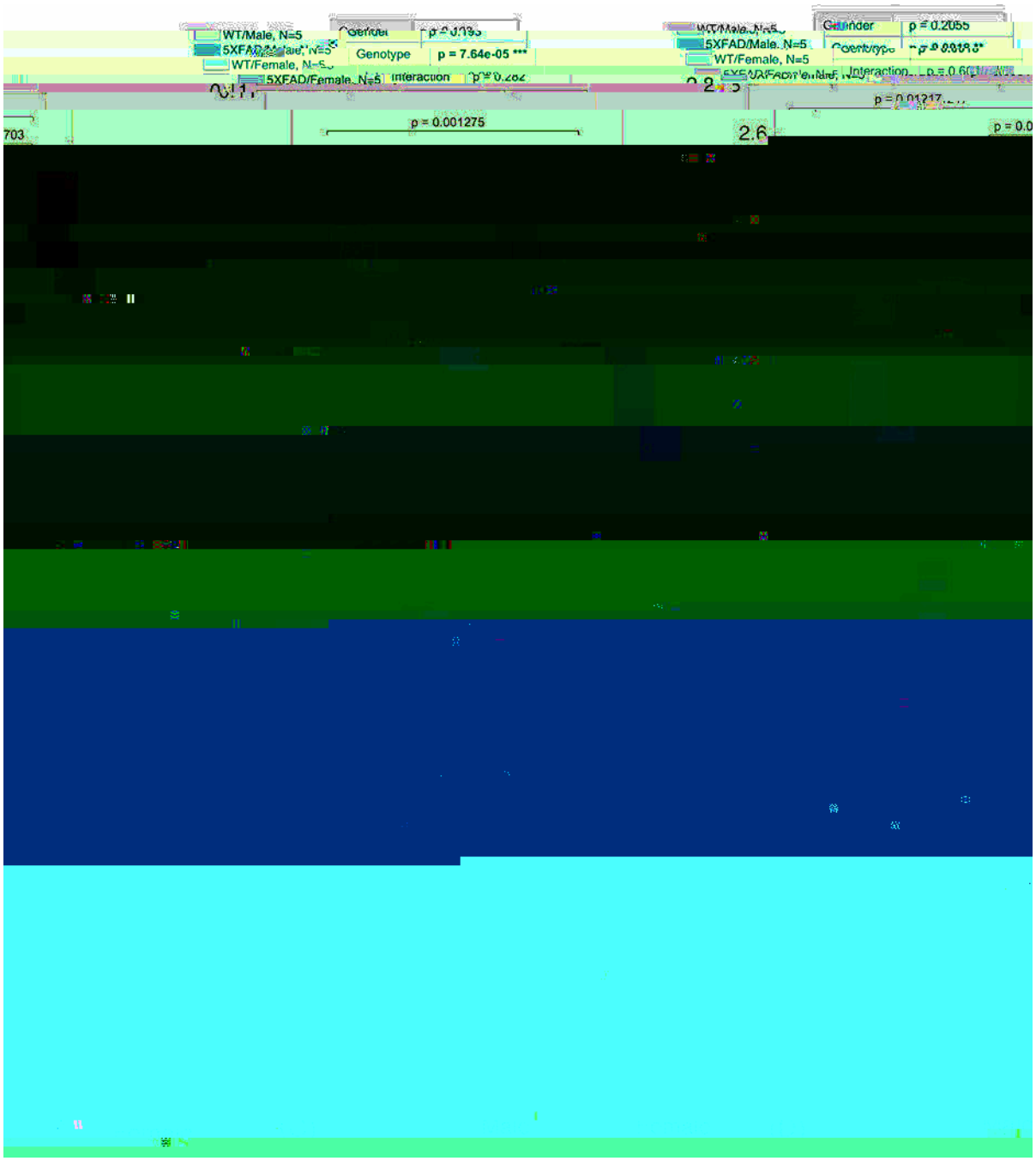

Figure 7. Loss of bone quality and diminished mineralization in 5XFAD mice.
(A) Crystallinity ($1/\nu_1PO_4^{3-}$). (B) B-type carbonate substitutions ($\nu_1CO_3^{2-}/\nu_1PO_4^{3-}$). (C) Mineral-to-matrix ratio ($\nu_1PO_4^{3-}$/Amide I). (D) Mineral-to-matrix ratio ($\nu_2PO_4^{3-}$/Amide

(95% CI) as post hoc tests in pairwise multiple comparisons procedure based on rank sums. Significant codes: $p < 0.05$ '*', $p < 0.01$ '**', $p < 0.001$ '***'.

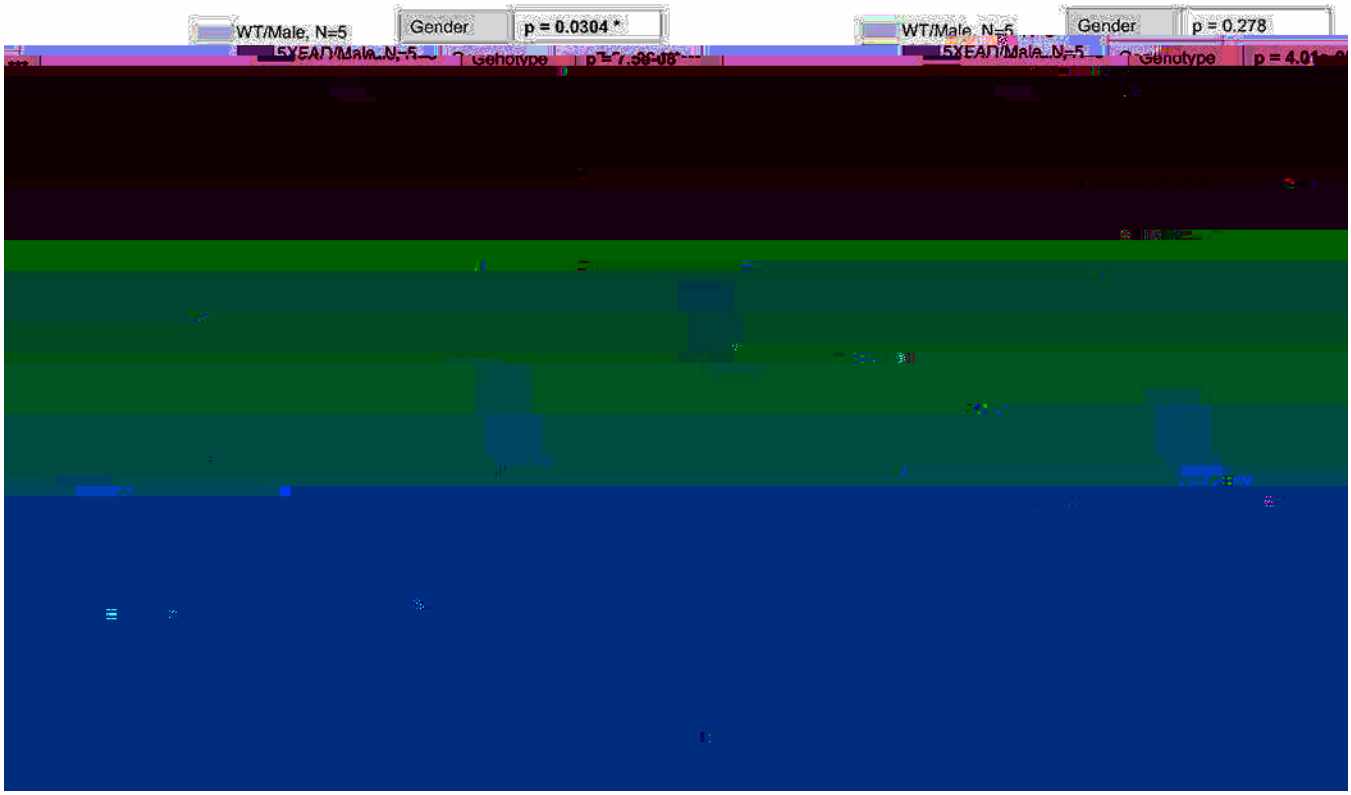

Figure 8. 5XFAD mice showed accumulation of glycoxidation products.

(A) Carboxymethyl-lysine (I_{1150}/CH_2-wag). (B) Pentosidine (I_{1495}/ CH_2-wag). Results are shown as boxplots (with median and interquartile range) showing all data points. Statistically significant differences were determined by Two-Factor ANOVA with Replication ($\alpha < 0.05$) to discern gender, genotype, and interactions effect, with Tukey's HSD test (95% CI) as post hoc tests in multiple comparisons of means. Significant codes: $p < 0.05$ '*', $p < 0.01$ '**', $p < 0.001$ '***'.

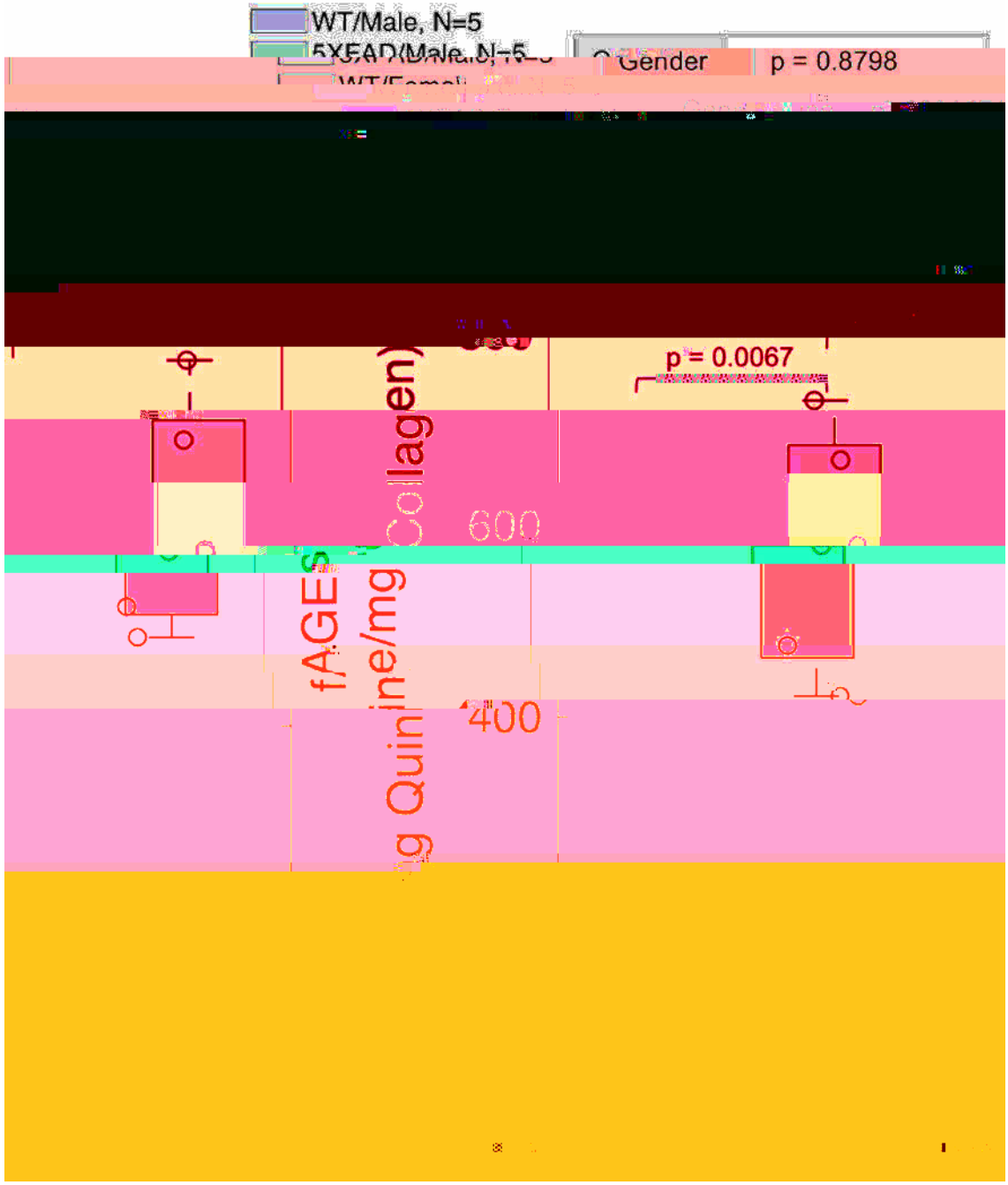

Figure 9. 5XFAD mice showed greater accumulation of fAGEs.

Results are shown as boxplots (with median and interquartile range) showing all data points. Statistically significant differences were determined by Kruskal–Wallis ($\alpha < 0.05$) test by ranks to discern gender, and genotype effects, with Dunn's test (95% CI) as post hoc tests in pairwise multiple comparisons procedure based on rank sums. Significant codes: $p < 0.05$ '*', $p < 0.01$ '**', $p < 0.001$ '***'.

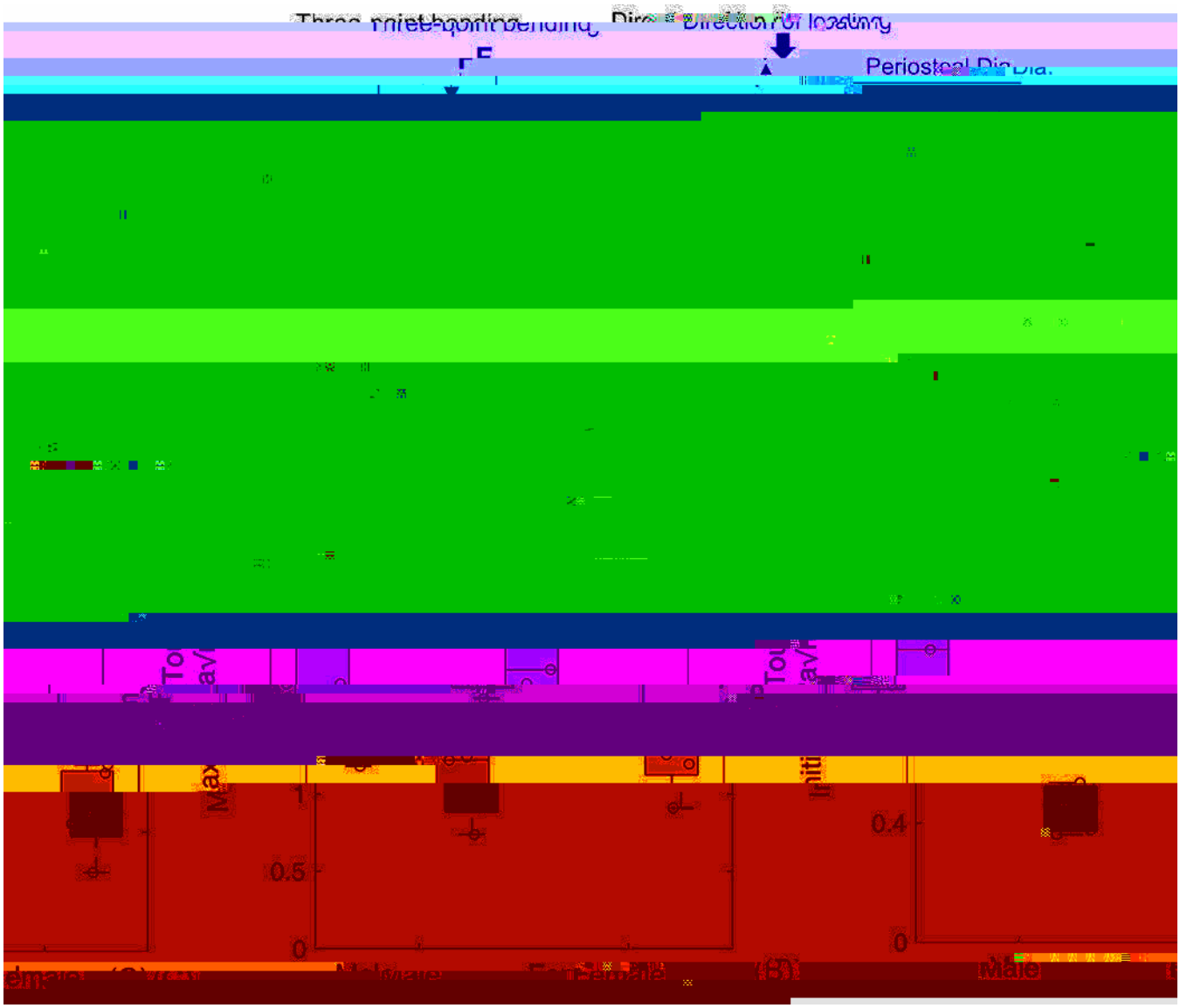

Figure 10. Loss of bone toughness in 5XFAD mice.

(A) Bone toughness was measured by subjecting femora to three-point bending. (B) Initiation toughness. (C) Maximum toughness. Results are shown as boxplots (with median and interquartile range) showing all data points. Statistically significant differences were determined by Two-Factor ANOVA with Replication ($\alpha < 0.05$) to discern gender, genotype, and interactions effect, with Tukey's HSD test (95% CI) as post hoc tests in multiple comparisons of means; or by Kruskal–Wallis ($\alpha < 0.05$) test by ranks to discern gender, and genotype effects, with Dunn's test (95% CI) as post hoc tests in pairwise multiple comparisons procedure based on rank sums. Significant codes: $p < 0.05$ '*', $p < 0.01$ '**', $p < 0.001$ '***'.

Table 2.

Correlation between selected structural, biomechanical, and compositional measures.

	Crystallinity	CO_3^{2-}/ PO_4^{3-}	MMR	Crystal Size	CML	PEN	fAGEs	Kc, in	Kc, max
Aβ	ρ = −0.65 **(0.001858)**	ρ = 0.56 **(0.01024)**	ρ = −0.77 **(6.86E-05)**	ρ = −0.68 **(0.000872)**	ρ = 0.82 **(8.82E-06)**	ρ = 0.87 **(7.64E-07)**	ρ = 0.87 **(7.64E-07)**	ρ = −0.78 **(4.42E-05)**	ρ = −0.59 **(0.006125)**
Crystallinity	1	r = −0.54 **(0.01306)**	r = 0.64 **(0.00235)**	r = 0.51 **(0.02183)**	r = −0.73 **(0.000229)**	r = −0.49 **(0.02724)**	ρ = −0.60 **(0.00656)**	r = 0.63 **(0.00302)**	ρ = 0.34 (0.141)
CO_3^{2-}/PO_4^{3-}		1	r = −0.42 (0.0686)	r = −0.41 (0.0697)	r = 0.61 **(0.00415)**	r = 0.24 (0.3149)	ρ = 0.72 **(0.0005407)**	r = −0.60 **(0.005297)**	ρ = −0.45 **(0.04901)**
MMR			1	r = 0.67 **(0.001101)**	r = −0.70 **(0.00057)**	r = −0.71 **(0.000445)**	ρ = −0.58 **(0.007973)**	r = 0.68 **(0.000868)**	ρ = 0.35 (0.1268)
Crystal Size				1	r = −0.72 **(0.000372)**	r = −0.60 **(0.00553)**	ρ = −0.63 **(0.003486)**	r = 0.69 **(0.000727)**	ρ = 0.30 (0.1925)
CML					1	r = 0.65 **(0.001961)**	ρ = 0.72 **(0.0005199)**	r = −0.81 **(1.4E-05)**	ρ = −0.49 **(0.0309)**
PEN						1	ρ = 0.75 **(0.0002206)**	r = −0.68 **(0.000894)**	ρ = −0.54 **(0.01538)**
fAGEs							1	ρ = −0.78 **(5.908e-05)**	ρ = −0.53 **(0.01673)**
Kc, in								1	ρ = 0.76 **(0.0001732)**

Coefficient of correlation determined by Pearson's R or Spearman's ρ for parametric or non-parametric, respectfully. Results are shown as correlation value (p-value). All groups were combined with N=20 (5/group; 50% Male/50% Female). Bold indicates statistically significant variable. Aβ = amyloid-βeta levels; CO_3^{2-} = carbonate; PO_4^{3-} = phosphate; MMR = mineral-to-matrix ratio; CML = carboxymethyl-lysine; PEN = pentosidine; fAGEs = fluorescent advanced glycation end-products; Kc, in = initiation toughness; Kc, max = maximum toughness.